Earth, Planets and Space

FULL PAPER Open Access

Variation of crater morphological parameters in the landing area of Tianwen-1: relationships with the geological environment and climate change

Yu Yang[1,2], Yi Wang[1], Bo Li[1*], Zongcheng Ling[1], Yang Liu[3], Shaojie Qu[4] and Shengbo Chen[2*]

Abstract

The Zhurong rover of the Tianwen-1 mission successfully landed in the southern part of the Utopian Planitia and the northern region of the dichotomy boundary. Craters within a ~ 134 km^2 region surrounding the Zhurong rover were identified and divided into seven degradation classes based on their preservation states and morphological details. Assessing how craters have degraded over time provides insight into local surface processes and then speculates on the climate evolution of the study area. The small depth/diameter (*d*/*D*) of craters in the study area may be caused by the rapid filling of sediments or by impact processes occurring in poorly cohesive weathering layers, and may also be associated with the volatile material alteration. As time went by, the process of crater degradation is nonlinear, and the degradation rate of the fresh crater in the study area at the initial stage of degradation may be as high as 0.2 m/Myr. The calculated surface erosion rate for the study area is ~ 10^{-2}–10^{-3} m/Myr, indicating that the erosion of the Martian surface since the Middle Amazonian occurred in the dry environment dominated by wind-sand erosion.

Keywords The Tianwen-1 landing area, The Utopia Planitia, Impact crater, Morphological parameters, Erosion rates

*Correspondence:
Bo Li
libralibo@sdu.edu.cn
Shengbo Chen
chensb@jlu.edu.cn
Full list of author information is available at the end of the article

Graphical Abstract

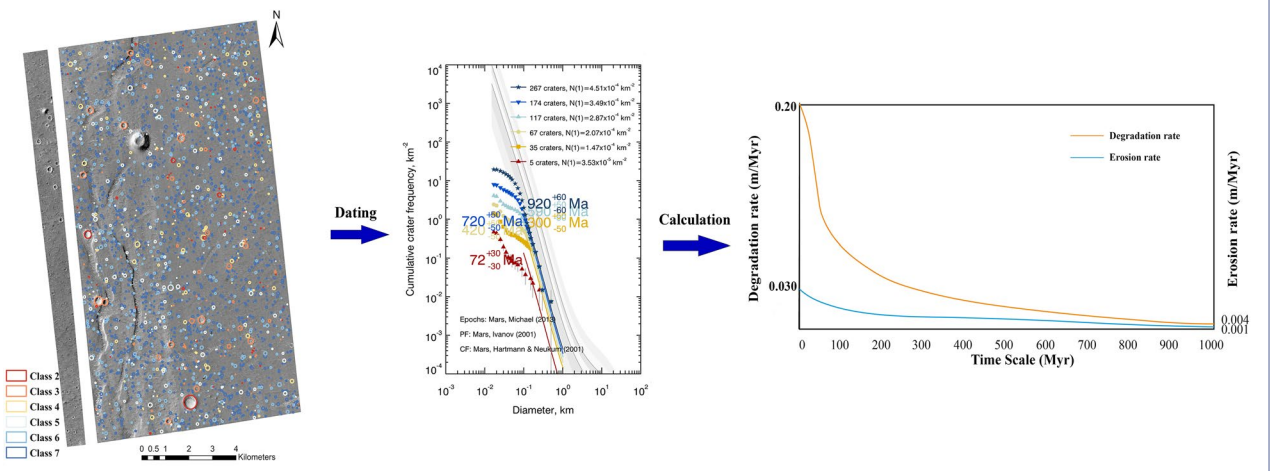

Introduction

The Zhurong rover of the Tianwen-1 mission successfully landed on May 15, 2021 (UTM+8) at 109.926°W, 25.066°N, in the southern part of the Utopia Planitia (Zou et al. 2021), north of the dichotomy boundary separating the southern Noachian highlands and the young northern lowlands. The Utopian Planitia has been interpreted as an ancient impact basin filled with a mixture of sediment, volatiles, or lava transported by water, wind, and other processes, and internally subjected to long-term modification and accumulation of late northern material (Searls et al. 2006). The landing site lies in the Late Hesperian lowland unit, dated to ~ 3.32–3.36 Ga, which consists mainly of Hesperian-epoch Vastitas Borealis formation (VBF) material (Tanaka et al. 2014). There are conical hills, wrinkle ridges, valleys, impact craters and other morphologies in the landing zone. The investigation of this region is of significant importance for in-depth human exploration and the study of Martian evolution and potential conditions for life.

The map (Fig. 1c) obtained by the High-Resolution Imaging Science Experiment (HiRISE) shows rocks and small craters in the Zhurong landing area. Numerous bright transverse aeolian ridges are visible in the image. The crater marked in Fig. 1c experienced severe erosion, characterized by heavily damaged rims, loss of clear impact structures, and an interior filled with fine-grained material. Its rim is surrounded by several dark rocks that may be spattered from the impact event. The surface traversed by the Zhurong rover is littered with small rocks and clasts bearing distinct features, including pitted surfaces and flake textures, which may indicate both the presence of physical weathering and aqueous interactions involving salt and brine (Ding et al. 2022; Liu et al. 2022). Thus, surface processes in this region may not be limited to impact gardening and weathering modification.

Impact craters are a dominant feature on Martian surfaces, while the morphology of small-scale craters is more sensitive to the strength and surface modification of the stratigraphy (Robbins and Hynek 2012). The causes and rates of crater degradation are spatially variable due to the variety of surface processes that have occurred and the complexity of local geological and climatic conditions (Michael and Neukum 2010). Consequently, studies of crater morphometry can be used to reveal the degeneration rate of craters in different Martian environments (Golombek et al. 2014). The High-Resolution Imaging Science Experiment (HiRISE) on board the Mars Reconnaissance Orbiter (MRO) (Mcewen et al. 2007) and the Digital Elevation Models (DEMs) derived from it (Kirk et al. 2008) allow a more quantitative characterization of crater shapes at small scales, which is important for a better understanding of the processes involved in crater formation and evolution.

In this study, craters with diameters greater than or equal to 19 m were identified using HiRISE images within a ~ 134 km^2 region (Fig. 2c) surrounding the Zhurong rover. Then craters were classified into seven degradation classes based on their preservation states and morphology features (rocks, bedforms, gaps, and superimposed craters), and their morphometric parameters were measured to determine the changes in erosion and degradation rates of craters over time using HiRISE-derived DEMs. This article is aimed at investigating the geological evolution of the Tianwen-1 landing area and the conducting research on the surface processes of Mars. Our

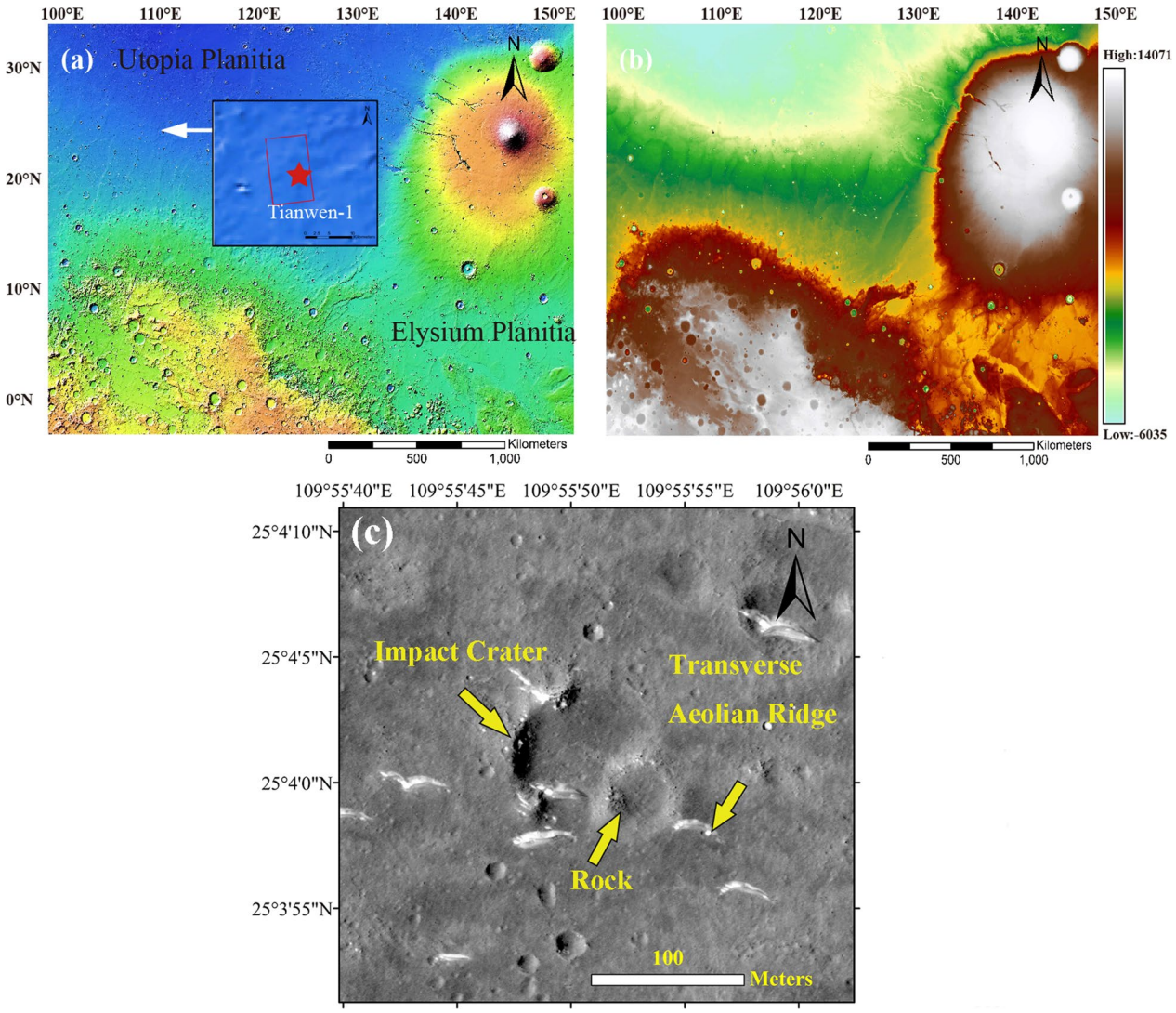

Fig. 1 **a** Geographical background and main geomorphological features of the Tianwen-1 landing site on a base map of Mars orbit laser altimeter (MOLA) (available at https://astrogeology.usgs.gov/search/map/Mars/GlobalSurveyor/MOLA). **b** Mars Global Surveyor MOLA DEM data. **c** is High-Resolution Imaging Science Experiment image (0.25 m/pixel), which shows craters, rocks, and transverse aeolian ridges (yellow arrows). Image ID ESP_ 069876_2055

goal in this study is to analyze the dependence of crater morphometric parameters on the geologic conditions at the Tianwen-1 landing site and to discuss the variation of crater's erosion and degradation rates on a long-time scale.

Data and methods

HiRISE data

The High Resolution Imaging Science Experiment (HiRISE) is one of the most advanced and sophisticated scientific payload carried on the Mars Reconnaissance Orbiter (MRO), which was launched by the U.S. in August 2005 (Johnston et al. 2003). This camera features a primary mirror with a diameter of 0.5 m, an effective focal length of 12 m, and a focal plane system. The integration of these cutting-edge components enables the HiRISE camera to capture exceptionally high-resolution images of the Martian surface. Furthermore, the HiRISE camera boasts an astonishing image acquisition speed, capable of capturing images containing 28 Gb of data in just 6 s. The HiRISE camera offers a spatial resolution of the 0.25 m/pixel, providing the capability to acquire highly detailed structural information within a small crater with accuracy down to the meter scale. This not only enables the measurement of changes in dune positions over time but also facilitates the detection of rock

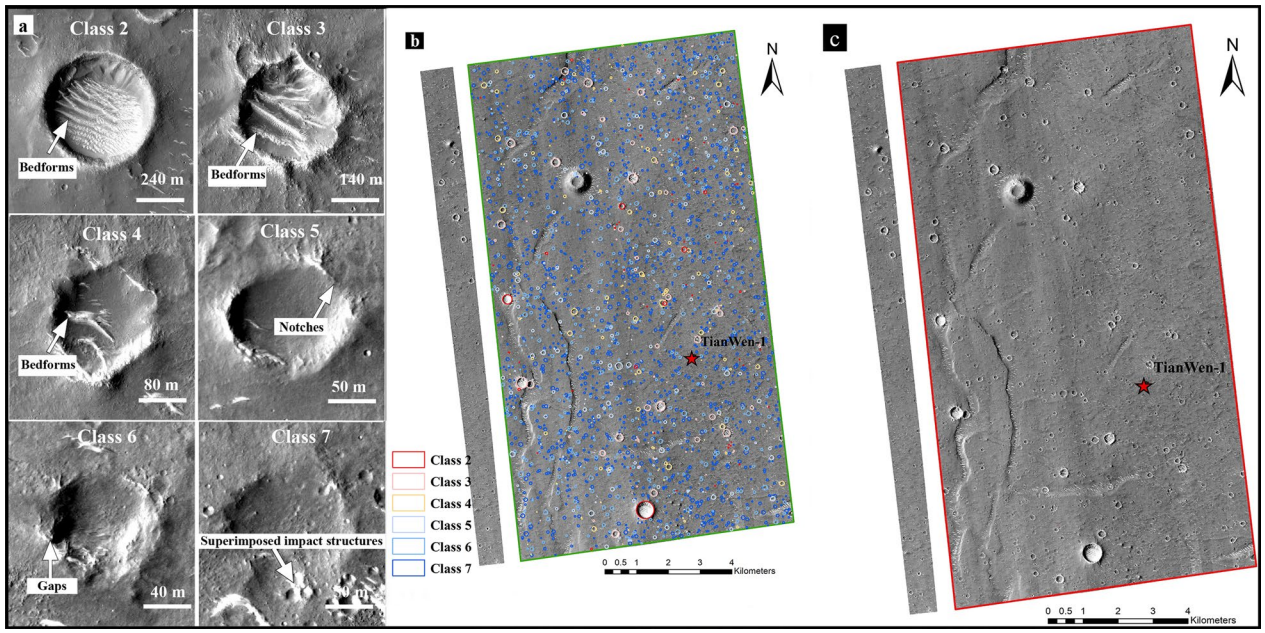

Fig. 2 **a** Six different morphological classes of craters in the study area. Some features are marked with white arrows. **b** The classification and spatial distribution of craters in HiRISE images ESP_069665_2055 and ESP_069876_2055. **c** Impact crater study area, indicated by the red box. The red pentagram represents the landing site of Tianwen-1

distributions resulting from impact crater ejecta, as well as the distinctive color characteristics of primary impact crater ejecta materials.

The HiRISE DTMs (Digital Terrain Models) are generated by the University of Arizona and the U. S. Geological Survey (USGS) using stereo imagery and the Softcopy Photogrammetric Engineering and Terrain (SOCET-SET) photogrammetric software, following the established USGS standard methods. The vertical accuracy of HiRISE DTM is tens of centimeters, which is sufficient to discern meter-scale rocks within impact crater ejecta, dunes on crater floors, and shallow pits covering crater walls.

Craters mapping

This paper used two HiRISE orthorectified images at 25 cm per pixel and HiRISE DTMs at 1 m grid spacing. DTM1 was produced by HiRISE stereo pair ESP_069665_2055 and ESP_069731_2055. And DTM2 was produced by HiRISE stereo pair ESP_069876_2055 and ESP_069942_2055 (Table 1). They are sufficient to identify rocks in the ejecta, bedforms on the crater floor, gaps in the crater rim, and shallow craters superimposed on the crater rim. Measured variations accurately reflect the intrinsic variation of the surface characteristics. A total of 2625 craters were identified and drawn using the CraterTools (a 3-point digitizing tool) (Kneissl et al. 2011). Obvious secondary impact craters that occur in clusters and chains were excluded. The morphological parameters of each crater, including the depth (d), height (h), and diameter (D), are measured to (1) determine crater changes over time and their degradation processes; (2) constrain crater degradation rates and surface erosion rates.

Table 1 HiRISE DTM data and associated stereopairs

DTM name	Stereopairs	
	Left	Right
DTEEC_069665_2055_069731_2055	ESP_069665_2055	ESP_069731_2055
DTEEC_069876_2055_069942_2055	ESP_069876_2055	ESP_069942_2055

Crater classification scheme

Each identified crater is classified according to its preservation states and morphological details. Watters et al. (2015) identified three classes of craters to understand how craters change over time on the Martian surface: Modif. Vis. Level 1 (MV1), Modif. Vis. Level 2 (MV2), and Modif. Vis. Level 3 (MV3). Warner et al. (2020) built a new classification scheme based on Sweeney et al. (2018)'s classification principles, expanding to smaller and more degraded Class 6 to 8 craters. In this paper, we recognize seven degradational states of craters in the Tianwen-1 landing area, as shown in Fig. 2a.

Class 1 craters exhibit well-defined low albedo rays (Daubar et al. 2013), and represent the ideal pristine state. They have sharply raised rims, steep inner walls, and distinctly bowl-shaped or flat-bottomed conical cavities. Dark sand is visible at the bottom of impact craters, with no superimposed impact craters above. No Class 1 crater was found in our study area.

Class 2 craters show elevated and well-defined rims, with a large number of sand-sized materials and bedforms migrating to and depositing in their floors (Fig. 2a, Class 2). There are a few superimposed craters within their ejecta blankets.

The floors of Class 3 craters become flat owing to the remarkable accumulation of bedforms, with more small craters superimposed on them (Fig. 2a, Class 3). Although the rims are elevated and maintain a round shape, gaps and notches appear on them. Bedforms are still evident on the crater floor, indicating that sand is migrating toward the crater floors, still featuring high albedo and reduced abundance.

Class 4 craters show gradually degraded and slightly elevated rims with more gaps and notches, obstructing a few bedforms (Fig. 2a, Class 4). Smooth infill completely covers the crater floors, where interior bedforms are rarely observed. The density of small impact structures superimposed around and within the Class 4 craters further increases.

Class 5 crater has a significantly eroded rim and is dominated by more gaps and notches (Fig. 2a, Class 5). Its floor is sandy and smooth, and the superimposed craters become denser and more degraded. Moreover, the Class 5 crater shows up a circular depression with a bright rim and dark interior. In craters composed of sandy, small impact features with well-defined edges are retained on the fill material, indicating its solidification. Regarding impact craters with rocky ejecta, within this category of degradation, the rocks within the ejecta blanket have undergone complete weathering and dissolution.

Class 6 crater's rim is almost destroyed, and the interior of the crater is very smooth and becomes a sandy depression. The exterior of elevated rim remnants still traps a small number of bedforms (Fig. 2a, Class 6). The quantity of overlaid small craters surpasses that of Class 5 craters.

Class 7 craters are the most degraded in the study area, and their rims were almost eroded away (Fig. 2a, Class 7). They are usually shallow depressions with circular, flat floors. But if the superimposed impact structures are large enough, the Class 7 crater's rim can be disrupted to show a sub-circularity shape.

Measurement of crater depth and rim height

Morphological parameters (depth and rim height) of craters were evaluated using the semi-automatic extraction method proposed by Sweeney et al. (2018). The crater depth (d) was determined as the topography measured from the crater rim's top to the crater floor's deepest part (Fig. 3a and Additional file 1: Fig. S1). That is the maximum difference between the overlying rim elevation 3D surface and HiRISE DEM of the bottom. The rim height (h) is defined as the height difference from the crater rim's crest to the initial pre-impact plain. The initial plain is created by converting the $1D$ buffer vector graphics file rim to points proportional to the diameter. Then a $0.2D$ ring buffer for each cratered edge is created

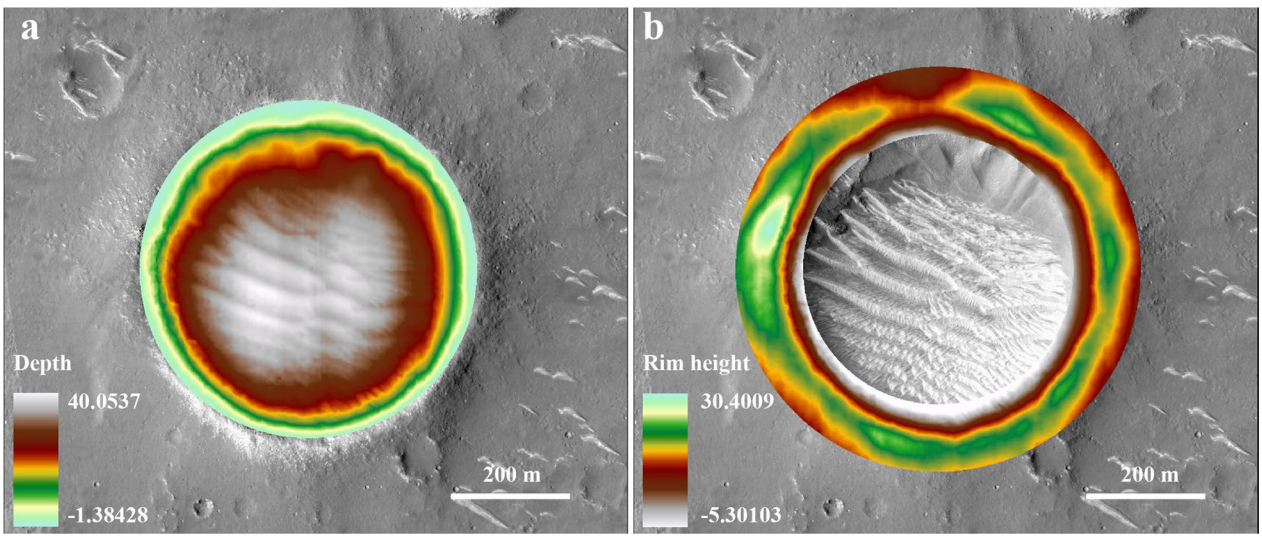

Fig. 3 Semi-automatic extraction results for morphometric parameters. HiRISE DEM shows the results of a class 2 crater (**a**) depth raster extraction and (**b**) rim height raster

because the rim width scales with diameter by approximately 0.2D. The rim height is the maximum difference between the initial plain surface and the 0.2D ring buffer (Fig. 3b and Additional file 1: Fig. S2). As the rim height measurements are highly disturbed by the surrounding terrain, impact craters fall in positive or negative terrain are excluded from the height analysis. As the rim height measurements are highly disturbed by the superimposed landform/transverse edge, or closing to the study region's boundary, impact craters are excluded from the height analysis.

Morphometric measurements analysis

The total number of identified craters in the study area is 2,625, including 63 Class 2 craters, 123 Class 3 craters, 138 Class 4 craters, 225 Class 5 craters, 515 Class 6 craters, and 1,561 Class 7 craters. Their diameters range from 19 to 553 m, among which small-diameter craters are dominant. However, because some of the impact craters were superimposed on other landforms or were close to the study area boundary, only 2,556 impact craters were measured for rim height.

Crater depth

Figures 4 and 5 illustrate the relationship between impact crater depth (d) and diameter (D), including the Class 2 to 7 craters, with diameter as the independent variable and the maximum depth as the dependent variable. For the Class 2 (Fig. 4a), 3 (Fig. 4b), and 4 (Fig. 4c), the linear fitting results for d/D are $d=0.070D$ ($R^2=0.97$), $d=0.060D$ ($R^2=0.94$), and $d=0.046D$ ($R^2=0.87$), respectively. For Classes 5 (Fig. 5a), 6 (Fig. 5b), and 7 (Fig. 5c), linear fitting results for d/D are $d=0.037D$ ($R^2=0.83$), $d=0.031D$ ($R^2=0.75$), and $d=0.021D$ ($R^2=0.60$), respectively. The linear fitting results of the crater depth (d) and diameter (D) for Class 2 to 7 are shown in Table 2.

The probability values (p value) of the linear fitting results are all below the 0.01 alpha threshold (Table 2), indicating that the effect of crater diameter on depth is extremely significant. There is an extremely significant statistical relationship between depth and diameter. In Figs. 4 and 5, it is clear that each class follows a positive linear trend consistent with the inferred crater degradation state, such that depth decreases as the degree of crater degradation decreases.

Height of crater rim

Figures 6 and 7 illustrate the relationships between crater rim height (h) and diameter (D), including Class 2 to 7 craters, with diameter as the independent variable and the maximum rim height of each crater as the dependent variable. The linear fitting results for Class 2 is $h=0.056D$ ($R^2=0.99$) (Fig. 6a), for Class 3 is $h=0.051D$ ($R^2=0.87$) (Fig. 6b), for Class 4 is $h=0.041D$ ($R^2=0.81$) (Fig. 6c). For Class 5 (Fig. 7a), Class 6 (Fig. 7b), and Class 7 (Fig. 7c), the linear fit of h/D is $h=0.031D$ ($R^2=0.63$), $h=0.025D$ ($R^2=0.32$), and $h=0.019D$ ($R^2=0.28$), respectively. The linear fitting results of the crater rim height (h) and diameter (D) for Class 2 to 7 are shown in Table 3.

As expected, the ratio between rim height to diameter generally decreases with increasing crater degradation class. However, compared to the relationship between depth and diameter, the maximum h/D illustrates scattering in the data. Also, the variation in rim height is less pronounced than the variation in depth for craters of all degradation classes. This may be due to the uneven degradation of the rim structure over time. It is found that peaks exist in the rim structure of even extremely degraded craters. Furthermore, it is also possible that the most proximal ejecta may be emplaced non-uniformly owing to irregularity in the initial topography of the target site, differences in target strength, or impact trajectory (Sweeney et al. 2018). In addition, the semi-automatic method of calculating crater rim heights is still strongly influenced by the topography of the surrounding plains, even if craters superimposed on other landforms and falling in apparently disturbed topography have been removed.

Correlations between crater depth and rim height

The histogram in Fig. 8a exhibits the distribution of d/D values for Class 2 to 7 craters. The highest d/D of all craters is derived from a Class 2 crater at 0.114. However, the largest h/D values do not result from the comparatively freshest Class 2 crater (Fig. 8b), which was an outlier that may be caused by the measurement method.

The relationships between h/D and d/D are shown in Fig. 8c with each crater labeled according to its membership in Class 2, 3, 4, 5, 6, and 7. The Pearson correlation coefficient (ρ) is quoted here to measure the correlation between h/D and d/D, and its value is between -1 and 1. The correlation is higher when it is closer to ± 1. The rim height and crater depth of Class 2 has a slight correlation with a $\rho=0.24$, whereas $\rho=0.20$ for craters in Class 3 and $\rho=-0.10$ for Class 4. For Class 5 to 7, ρ is 0.13, 0.05 and 0.07, separately.

Crater retention ages and modification rates

Time series of crater degradation

In this paper, the cumulative distribution function is used to determine the absolute model ages of the craters. The crater size-frequency distribution (CSFD) is binned in a pseudo-log manner, and the resurfacing correction method is used to determine cumulative model ages, mitigating the influence of a small number of large-diameter impact craters on the absolute model

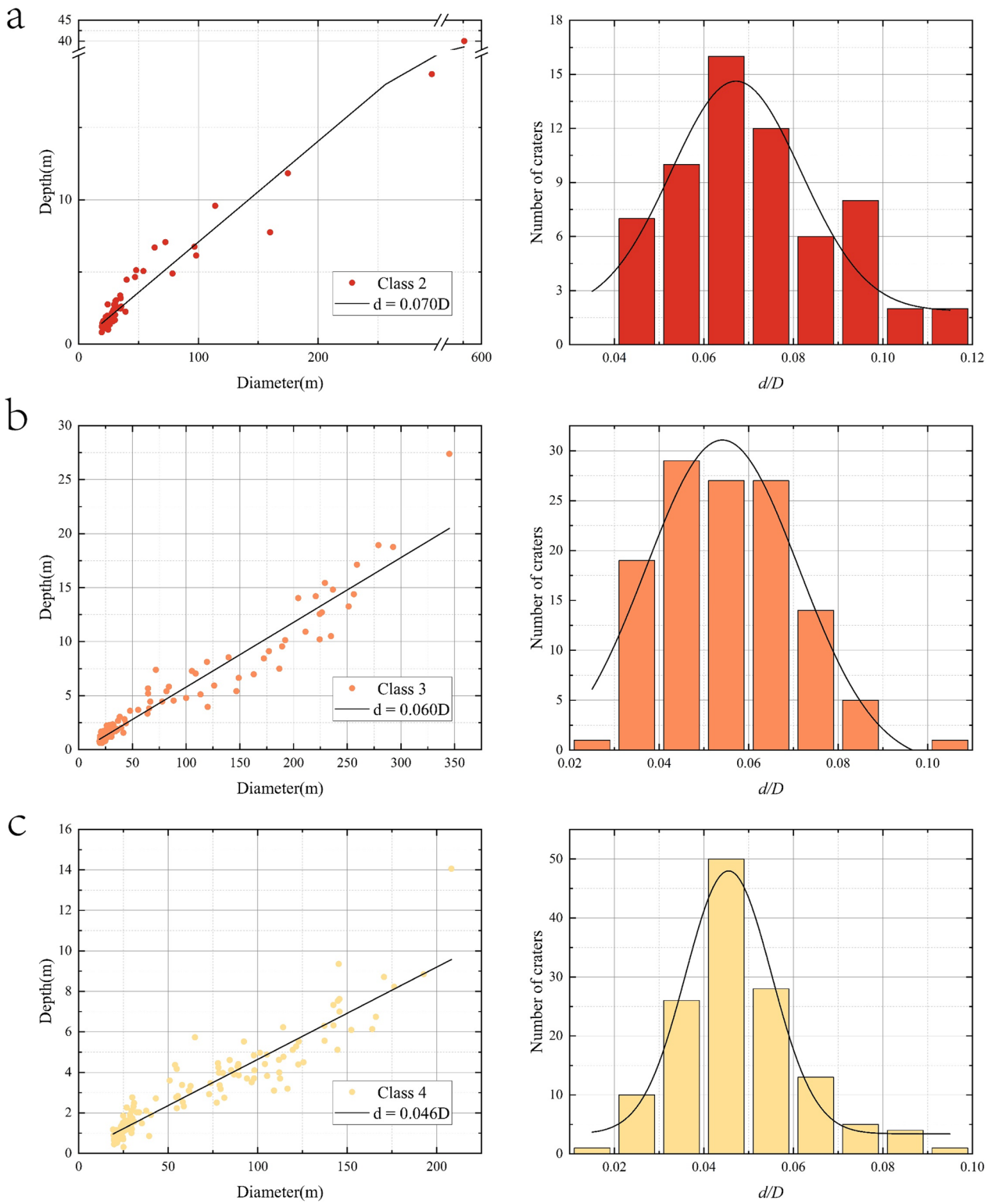

Fig. 4 The relationship between impact crater depth and diameter. **a**–**c** Unbinned maximum depth versus diameter plot showing Class 2 to 4 craters. Histograms of the distribution of *d/D* values for each Class are presented separately

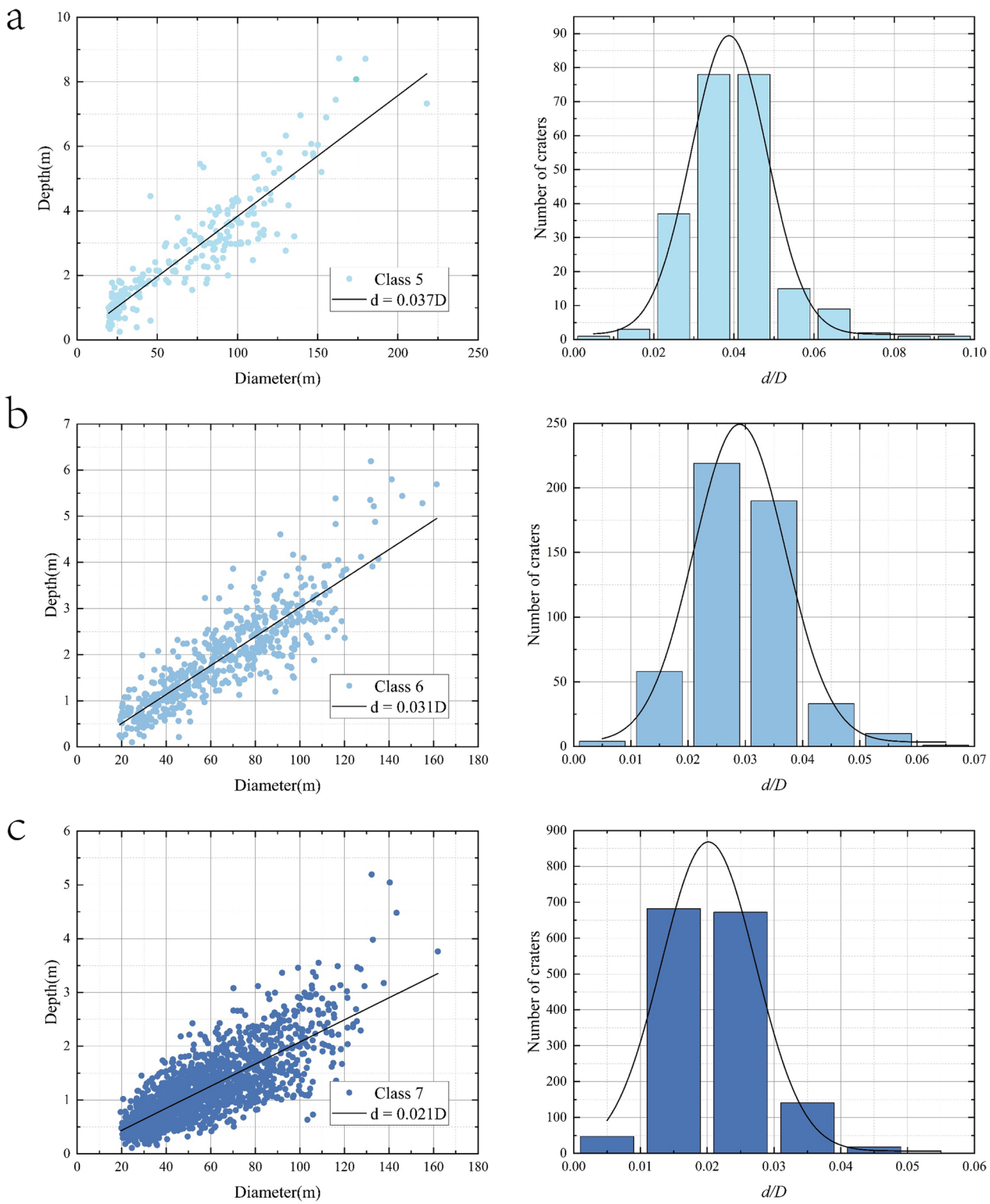

Fig. 5 Crater morphometric results relate maximum depth to crater diameter. **a**–**c** Unbinned maximum depth versus diameter plot showing Class 5 to 7 craters. Histograms of the distribution of *d*/*D* values for each class are presented separately

Table 2 Linear fitting results of depth vs. diameter

Class	2	3	4	5	6	7
Number	63	123	138	225	515	1561
R^2	0.97	0.94	0.87	0.83	0.75	0.60
P value	$1.95E^{-50}$	$1.08E^{-73}$	$1.25E^{-62}$	$1.10E^{-86}$	$2.22E^{-157}$	0
Standard Deviation	0.89	1.24	0.83	0.70	0.50	0.04
Equation	d = 0.070D	d = 0.060D	d = 0.046D	d = 0.037D	d = 0.031D	d = 0.021D

ages. The cumulative crater size-frequency functions for Class 1 to 2, 1 to 3, 1 to 4, 1 to 5, 1 to 6, and 1 to 7 craters are shown in Fig. 9. The size-frequency distributions (SFD) of craters in each class bin provides a generalized retention timescale for each class and allows for an assessment of the rates at which craters degrade from one class to the other (Golombek et al. 2014). Model age fits were constructed using the chronology function (Hartmann and Neukum 2001). The cumulative model ages are 920 ± 60 Ma for all 267 craters with $D \geq 100$ m (Class 1 to 7), 720 ± 50 Ma for Class 1 to 6 craters (174 craters), and 590 ± 50 Ma for Class 1 to 5 craters (117 craters). Also, the cumulative data provide a model age of 420 ± 50 Ma for Class 1 to 4 craters (67 craters), 300 ± 50 Ma for Class 1 to 3 (35 craters), and 72 ± 30 Ma for Class 1 to 2 (5 craters).

The distribution for craters ($D \geq 100$ m) follows a −3.2 power-law slope, similar to the crater production function (Ivanov 2001). It indicates that impact craters above this size are still preserved. As a result, a fit to the Class 1 to 7 grouping provides a general crater retention age for craters ($D \geq 100$ m). For craters ($D < 100$ m), the slope of the distribution crosses multiple isochrones, indicating that this population has been significantly eroded since the original surface formed. Model ages derived from the $D < 100$ m population represent the ability of the landscape to retain craters over specific exposure timescales.

Ages derived from the cumulative size-frequency distribution of Class 1 to 7 craters with $D \geq 100$ m confirm similar Middle Amazonian model ages of 920 ± 60 Ma to 970 ± 60 Ma for the study area. The age is much younger than the ~3.6–3.5 Ga absolute model age of the VBF unit obtained by Ivanov et al. (2014). It indicates that a later resurfacing process has occurred in our study area in the Middle Amazonian. We, therefore, focus on two distinct crater populations recorded in the Tianwen-1 landing area, a 10 m-scale crater population, and a 100 m-scale crater population that could reflect this resurfacing event. Crater retention ages derived from the cumulative method for the two populations were used to constrain the degradation/erosion rates below.

Degradation and erosion rates of craters

The decrease of Martian crater's d/D with time is mainly due to the filling by the migration of wind and sand deposits, the lowering of the rim height, and the backwasting effect of the crater walls. Therefore, the rate derived from the change in depth is defined as the crater degradation rate. In contrast, the decrease in crater's h/D with time is due to rim softening and rounding effects caused by some surface processes (e.g., eolian abrasion), which can be more closely tied to a true surface erosion rate (Sweeney et al. 2018). We quantified the variation in crater depth and rim height. Based on the model age for each class, we can determine the modification rates between crater classes.

Crater degradation and erosion rates for 100 m-diameter bins are shown in Table 4. Since the statistics for Class 1 and 2 craters are poor and the time intervals between classes are not well-constrained, we focus mainly on Class 3 to 7 craters. The 100 m-diameter craters in the Tianwen-1 landing area degrade from Class 3 to 7 craters over a time span of about 620 Myr, with their average depth decreasing from 6.38 m to 2.06 m at an average degradation rate of 0.007 m/Myr, while their rim height decreases from 3.42 m to 2.20 m at an average erosion rate of about 0.002 m/Myr. The degradation rate from Class 3 to 4 is approximately 0.018 m/Myr over a 120 Myr interval, whereas this rate is steady at 0.003–0.005 m/Myr for Class 4 to 7. The erosion rate between Class 3 and 7 remains essentially unchanged and stabilizes around the mean value (0.001–0.004 m/Myr). By comparison to the depth-related degradation rates, rim erosion rates for all craters are typically an order of magnitude lower between the younger class intervals. The degradation rates for each class interval in Table 3 reveal that craters degrade more rapidly in the earlier stages of modification. Furthermore, the time scale for distinguishing each class is not equal, implying a nonlinear decrease in the degradation rate over time. The error calculation formula for the degradation rate is

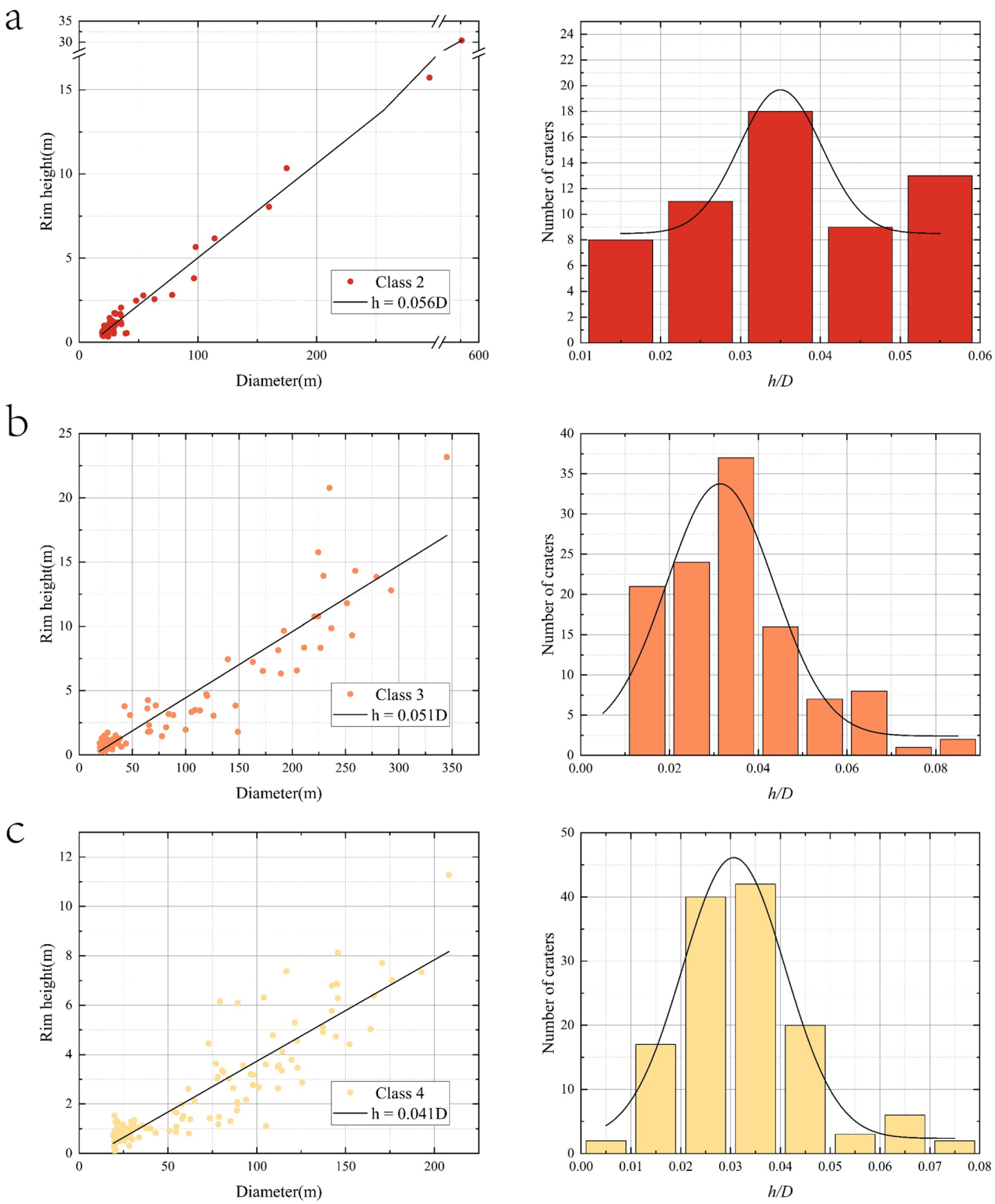

Fig. 6 Crater morphometric results relate maximum rim height to crater diameter. **a**–**c** Unbinned maximum rim height versus diameter plot showing Class 2 to 4 craters. Histograms of the distribution of *h/D* values for each Class are presented separately

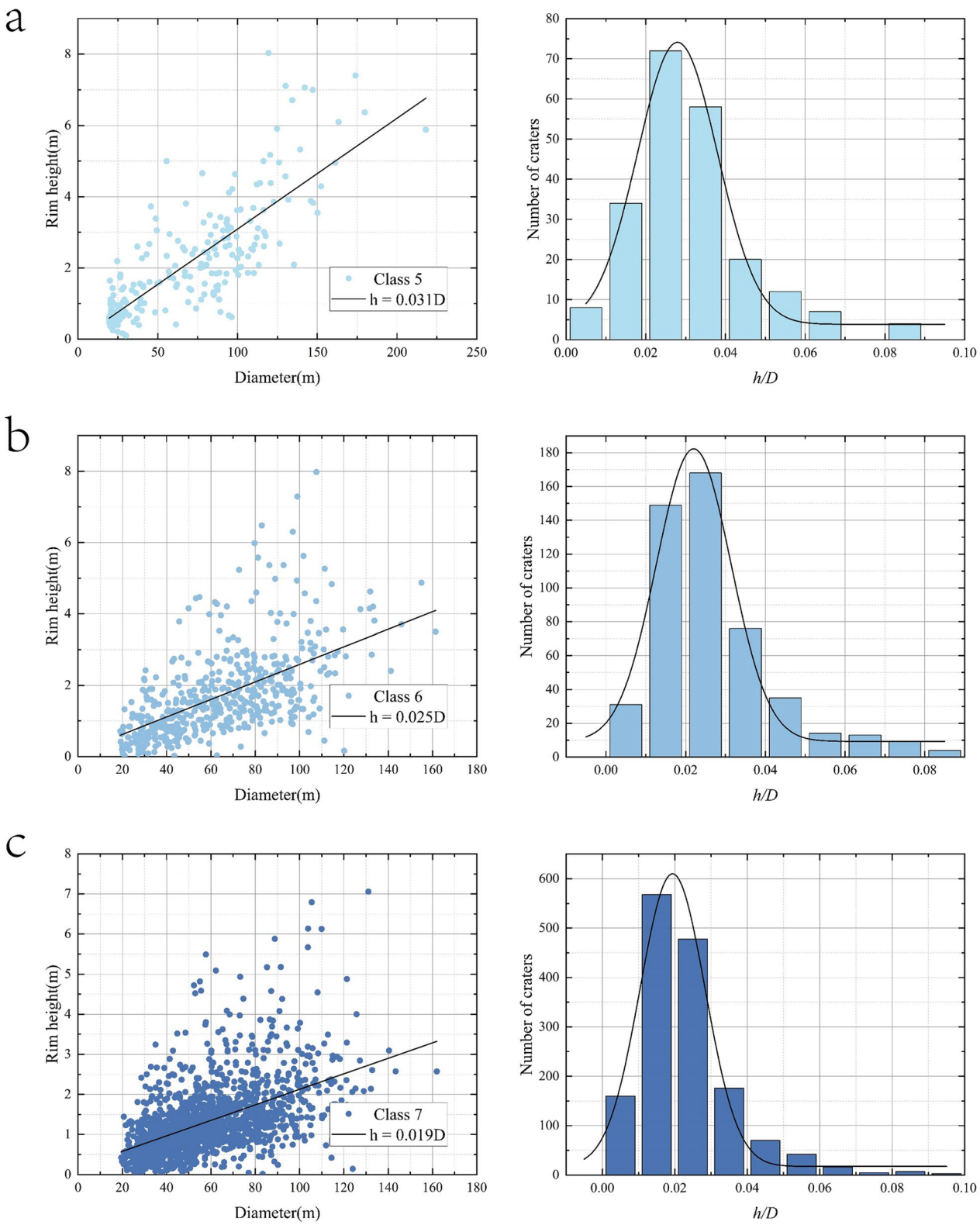

Fig. 7 Crater morphometric results relate maximum rim height to crater diameter. **a**–**c** Unbinned maximum rim height versus diameter plot showing Class 5 to 7 craters. Histograms of the distribution of *h/D* values for each Class are presented separately

Table 3 Linear fitting results of rim height vs. diameter

Class	2	3	4	5	6	7
Number	59	116	132	215	499	1525
R^2	0.99	0.87	0.81	0.63	0.32	0.28
P value	$1.30\ E^{-59}$	$9.16E^{-52}$	$5.91E^{-49}$	$4.52E^{-48}$	$1.05E^{-43}$	$7.14E^{-109}$
Standard Deviation	0.44	1.61	0.95	0.97	0.99	0.74
Equation	h = 0.056D	h = 0.051D	h = 0.041D	h = 0.031D	h = 0.025D	h = 0.019D

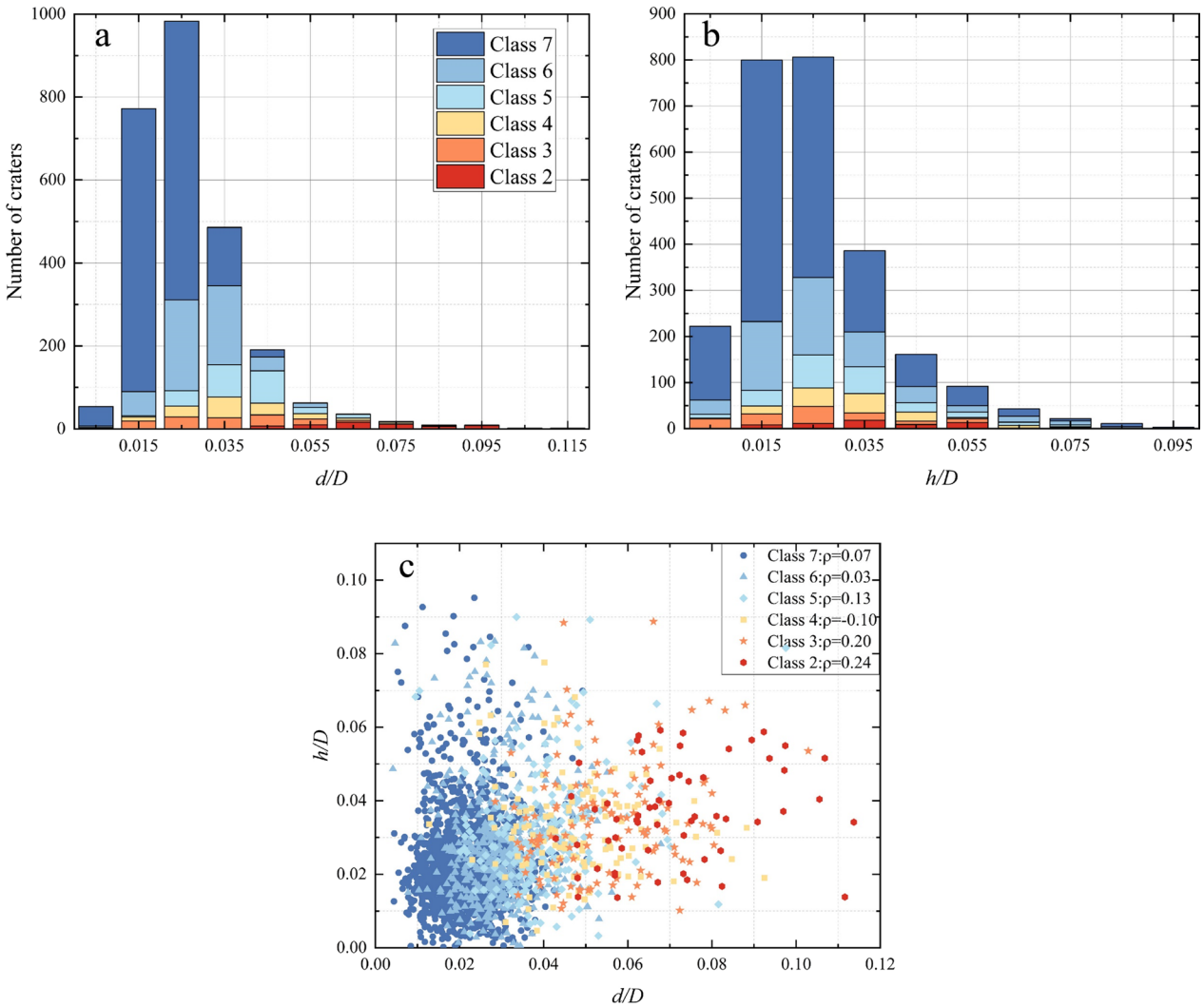

Fig. 8 **a** The number of craters per diameter-normalized depth, (**b**) the number of craters per diameter-normalized rim height. **c** The plot of diameter normalized rim height versus diameter normalized depth

$$DE_{i,k} = \frac{dSE_i + dSE_{i+1} + \cdots + dSE_k}{T_{i,k}} \quad (1)$$

where $DE_{i,k}$ represents the degradation rates for Classes i to k, dSE_i denotes Standard Error of depth for Class I, $T_{i,k}$ is time intervals between Class i and k from the cumulative fits. The erosion rate error is calculated in the same way.

Since the number of 100 m-diameter craters available for rim height analysis is so small in each class that the

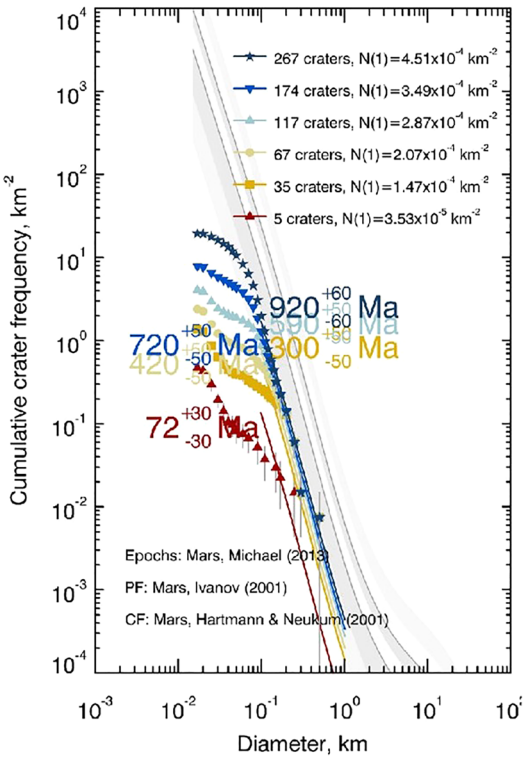

Fig. 9 Cumulative and size-frequency distributions for Class 1 to 7 craters in the study area. Class 1–7 craters (dark blue 5-pointed stars), Class 1–6 craters (blue inverted triangles), Class 1–5 craters (light blue triangles), Class 1–4 craters (yellow circles), Class 1–3 craters (orange squares), and Class 1–2 craters (red triangles). Cumulative crater SFD plots for Class 1 to 7 craters with pseudo-log bins. Hartmann and Neukum's (2001) chronology function and Ivanov's (2001) production function (gray line) are plotted, with gray areas indicating epoch boundaries (Michael 2013)

variation in rim heights is difficult to constrain. Here we introduce the above h/D linear fitting results (Figs. 5 and 6) for the 100 m-diameter crater rim erosion rate analysis. The linear fitting results for the rim heights of craters of Class 3 to 7 are $h=0.051D$, $h=0.041D$, $h=0.031D$, $h=0.025D$ and $h=0.019\cdot$, in that order. Then, based on the fitted values, the rim heights of 100 m-diameter craters of Class 3 to 7 are 4.1 m, 3.1 m, 2.5 m and 1.9 m, respectively. Thus, the modification of a 100 m-diameter crater from Class 3 to Class 4 implies an erosion rate of 0.008 m/Myr over ~ 120 Myr. The rim erosion rate was 0.006 m/Myr for Class 4 to 5, 0.005 m/Myr for Class 5 to 6 within 130 Myr, and 0.003 m/Myr for Class 6 to 7. Similar to the depth degradation rate, the rim erosion rate decreased between classes, and was generally 1 to 2 orders of magnitude lower than in the early and middle stages of degradation.

Crater degradation rates for Class 2 to 7 with diameters range from 50, 60 to 80 m are provided in Table 5. For craters with a diameter of tens of meters, the degradation rate from Class 2 to 3 is about 0.07 m/Myr, from Class 3 to Class 4 is about 0.013–0.018 m/Myr, and between Class 4 and 5 the degradation rate decreases to 0.005–0.014 m/Myr. While between Class 5 and 6 the degradation rate is basically stable between 0.002–0.004 m/Myr, and between Class 6 and 7 the degradation rate was approximately 0.001 m/Myr. Likewise, this also indicates that craters degrade more quickly in the earlier stages of modification. The overall trend of the calculated degradation rates indicated a decrease with time. And in the final stage of degradation, the erosion rate and degradation rate are similar probably because the filling process in craters no longer plays an important role.

However, there is no noticeably faster degradation rate exhibited in 50 m-diameter craters relative to the order of the 100 m-diameter population. Assuming that craters are filled from their original depth (0.2 times their diameter) and an average fill rate of 0.02 m/Myr. It takes about 500 Myr for a 50 m-diameter original crater to degrade to Class 7, and about 1000 Myr for a 100-m-diameter original crater to the most degraded class. In Table 5 the 50- to 60 m-diameter Class 7 craters have a maximum retention time of about 640 Myr and a maximum retention age of about 1100 Myr for the 100 m-diameter craters. This is probably because the degradation of craters in this diameter range is dominated by material filling and other processes do not play a significant role.

Discussions

Dependence of morphometric parameters on the geological environment

Simple fresh impact craters on rocky planets are typically bowl-shaped, with a depth-to-diameter ratio of ~ 0.20 and rim height-to-diameter ratio of ~ 0.04 (Pike 1977; Melosh 1989). Daubar et al. (2014) counted an average depth-to-diameter ratio of about 0.23 for the meter-to decimeter-scale craters identified on Mars over the last two decades. The depth-to-diameter ratio of secondary craters (about 0.1) appears to be half that of the primary craters (Pike and Wilhelms 1978). Garvin et al. (2003) found that simple craters followed a relationship of $d=0.196D^{0.96}$ and $h=0.03D^{0.96}$. As can be seen in Fig. 10a, only a portion of the Class 2 craters and one Class 3 crater have d/D exceeding 0.1. However, this is far below the previously studied results for fresh craters with $d/D=0.2$. While a sizeable portion of craters in each class has rim height-to-diameter ratios exceeding 0.04 (Fig. 10b).

Stewart and Valiant (2006) suggest that the power law applies to the depths of the deepest craters and the rims of the highest craters. And Robbins and Hynek (2012) proposed a "deepest crater" approach, where the power law fits the deepest craters in a set of diameter bins.

Table 4 Degradation and erosion rate data for 100-m-scale craters

Class	Crater diameter bin (90 to 110 m)							
	n	*d*	Standard Deviation	Standard Error	*n*	*h*	Standard Deviation	Standard Error
3	3	6.38	1.12	0.65	2	3.42	0.08	0.06
4	11	4.24	0.71	0.21	11	3.29	1.29	0.39
5	35	3.49	0.60	0.10	34	2.69	0.88	0.15
6	71	2.78	0.63	0.07	70	2.54	1.46	0.17
7	116	2.06	0.64	0.06	112	2.20	1.15	0.11

Class interval	Time interval (Myr)	Degradation rate (Dr) (m/Myr)	Dr Error	Erosion rate (Er) (m/Myr)	Er Error
3–4	120	0.018	0.007	0.001	0.004
3–5	290	0.010	0.003	0.003	0.002
3–6	420	0.009	0.002	0.002	0.002
3–7	620	0.007	0.002	0.002	0.001
4–5	170	0.004	0.002	0.004	0.003
4–6	290	0.005	0.001	0.003	0.002
4–7	500	0.004	0.001	0.002	0..02
5–6	130	0.005	0.001	0.001	0.002
5–7	330	0.004	0.001	0.001	0.001
6–7	200	0.003	0.001	0.002	0.001

Accordingly, we extrapolate the scaling law $d = cD^m$ from large simple craters on Mars to a small diameter range by fitting the three deepest craters in 10-diameter bins. The fitting result is $d = 0.187D^{0.775}$ (Fig. 10c). It is smaller than the result of Stewart and Valiant (2006) ($d = 0.288D^{0.790}$) for new craters on the Utopian Planitia with craters' diameters ranging from 3 to 50 km. A least-squares power fit to the three largest rim heights in 10-diameter bins yielded a result of $h = 0.232D^{0.710}$ (Fig. 10d). It can be noticed that the fitting results are overall greater than $h = 0.04D$. The reasons for the discrepancies between our fitting results and previous studies are discussed in detail as below:

(1) Nonlinear degradation processes of craters. It is evident in "Crater retention ages and modification rates" section that a marked decrease in the degradation rate of craters occurs as the degree of degradation increases. The pristine crater exposes mixed coarse- and mostly fine-grained ejecta deposits that are in disequilibrium with local geomorphic thresholds and have undergone relatively rapid degradation by eolian and lesser mass-wasting processes (Golombek et al. 2014; Grant et al. 2020). After early crater infilling, degradation rates greatly slowed. This is mainly attributed to the fact that the inventory of available fines for transport from the crater rim into the floor became limited. Additionally, it may be owing to the very slow weathering of resistant basaltic rocks in and around craters (Grant et al. 2020). Moreover, longer-term surface stability was enhanced as almost complete infilling reestablished a surface profile close to equilibrium with local winds. As a result, the d/D of the original crater may decline rapidly during the early stages.

(2) Secondary Craters. The distant secondary meteorite is produced by the high-speed ejecta and will hit the surface at a low impact speed, which can form small, round, isolated craters (Daubar et al. 2014). Statistically, the d/D ratios of the identified craters are fairly close to those of typical secondaries. There are no craters with d/D ratios up to 0.2. It is hard to determine whether the crater is primary or secondary when small craters are far from the main crater.

(3) (3) Geological Conditions. Martian impact structures are sensitive to target properties and local depositional processes (Garvin et al. 2003). Zhao et al. (2021) proposed a five-layer stratigraphic model of the Tianwen-1 landing zone based on observations and previous studies. This model provides a framework for studying the geologic evolution of the region. According to the model, the top layer consists of relatively loose material, less than 48 m thick, followed by the second layer consisting of coarser and rockier material. However, small-diameter craters are able to excavate the rego-

Table 5 Data derived from the crater statistics (Fig. 10a) at $D = 50$, 60, and 80 m, including the number, model ages, and error information as well as the degradation rate calculated based on the model age

D(m)	1–2			1–3			1–4			1–5			1–6			1–7		
	N	Age (Ma)	Error (Ma)	N	Age (Ma)	Error (Ma)	N	Age (Ma)	Error (Ma)	N	Age (Ma)	Error (Ma)	N	Age (Ma)	Error (Ma)	N	Age (Ma)	Error (Ma)
Cumulative data																		
50–60	1	4.9	1	2	24	3	11	54	5	19	110	7	70	260	10	306	640	20
60–70	1	8	2	6	41	6	10	88	8	22	190	10	83	410	20	270	900	30
80–90				3	82	10	12	180	20	36	370	30	92	680	40	206	1200	50

D (m)	Crater degradation rates (m/Myr)				
	2–3	3–4	4–5	5–6	6–7
50–60	0.071	0.018	0.014	0.004	0.001
60–70	0.066	0.015	0.012	0.003	0.001
80–90		0.013	0.005	0.002	0.002

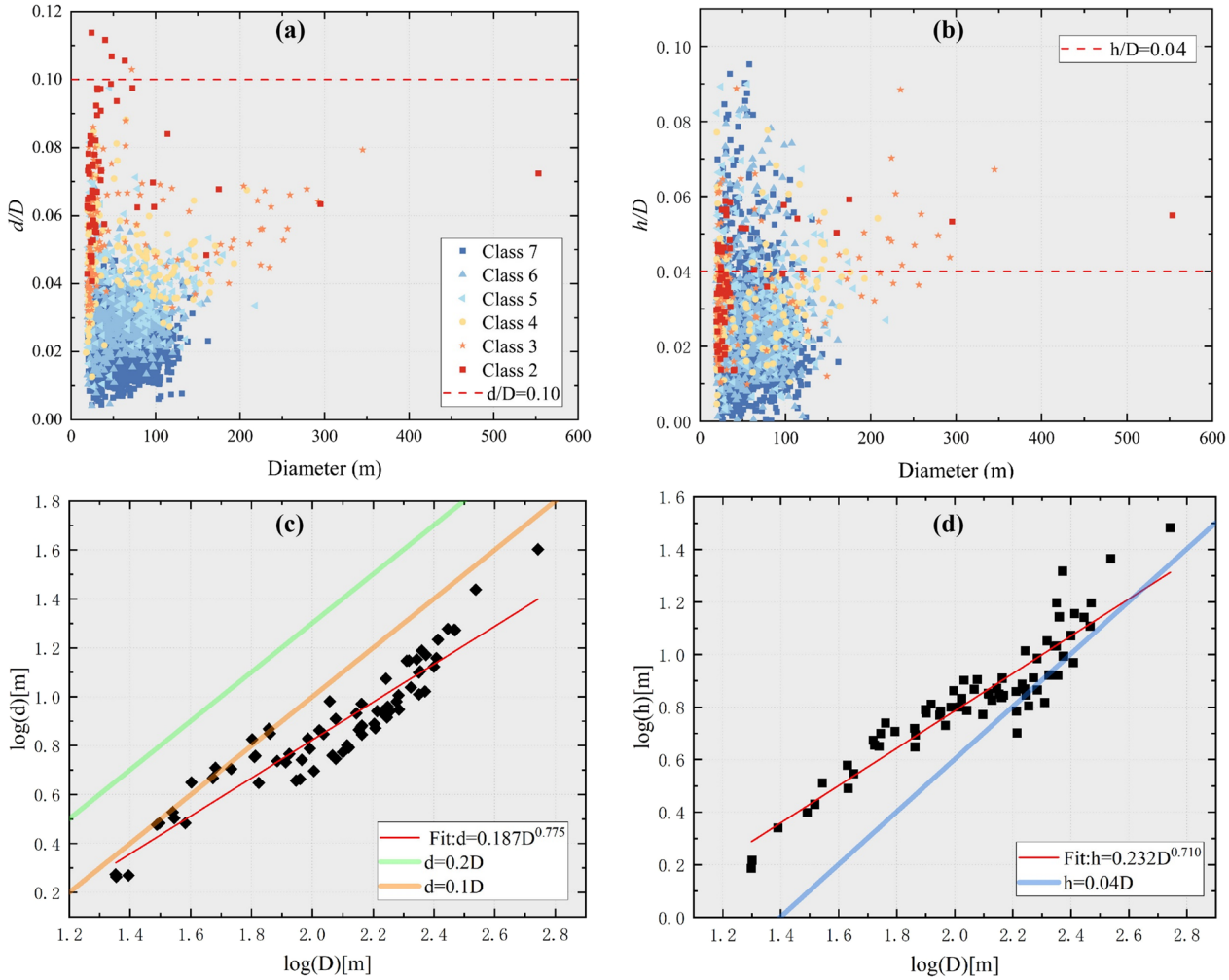

Fig. 10 **a** Depth to Diameter (*d*/*D*) plotted against diameter for each measured crater, and the red dashed line with *d*/*D* = 0.10 is listed for comparison. **b** Diameter plotted versus *h*/*d* for each measured crater. The trend of *h*/*D* = 0.04 (red dashed line) is shown for comparison. **c** *d*/*D* power-law fits for the three deepest craters in 10-diameter bins (solid red line), with the light green line at *d* = 0.2*D* and the light orange line at *d* = 0.1*D* (Fit: N = 72). **d** A line (solid red line) was fitted to the three largest rim height craters in 10-diameter bins (Fit: N = 71). The trend of *h*/*D* = 0.04 (light blue line) is also labeled for comparison

lith but not the more competent bedrock beneath it, resulting in a smaller crater that marks contact with the more resistant unit. Therefore, the lower *d*/*D* of craters in the study area may be caused by impact events that arise in poorly cohesive surficial regolith. Li et al. (2022) shows that the Zhurong rover's radar reveals the shallow subsurface structure of the Mars Utopia Planitia. They divided the subsurface structure into four layers The first layer is no thicker than 10 m, containing of mainly regolith (Additional file 1: Fig. S3). Zaki et al (2023) have found that potential episodic warming punctuated the climate of early Mars during the Late Noachian to Early Amazonian (~3.7 to > 2.4 Ga). In addition, Stewart and Valiant (2006) found shallow, primitive impact craters on volatile-rich surfaces. Thus, the prevalence of shallow craters in the landing zone may be related to volatile action.

In summary, the small *d*/*D* of craters in the study area may be due to the rapid filling of early craters, or due to the fact that the impacts occurred on cohesionless or poorly consolidated surface weathered layer material, or may be related to volatiles. Subsequent ground penetrating radar data from the Zhurong rover and directional

studies of the Tianwen-1 may provide more detailed evidence and explanations.

Changes in degradation and erosion rates over time

Under the natural state, craters undergo degradation processes from formation to complete disappearance, and the time of the whole degradation process is the total life cycle of craters. The degradation and erosion rate schedules for the craters in Fig. 11 are calculated based on the Table 4. Due to the low number of Class 1 and 2 craters in the study area, the degradation rates for relatively fresh Class 1 and Class 2 craters are determined by subtracting the observed crater depth from the original crater depth (0.2 times the diameter) and dividing it by the age of the crater. While crater degradation rates for Class 3 to 7 craters used previously calculated values. And the erosion rate of Class 1 and 2 craters is estimated by dividing the difference between the rim depth result $h = 0.232D^{0.710}$ fitted in this paper and the actual calculated rim height of Class 1 and 2 craters by the retention age. Fresh craters degrade rapidly in the early post-impact period, possibly at a rate of 0.2 m/Myr (Fig. 11). Over time, the degradation rate decreases by two orders of magnitude and reaches stability. Between the first 100 Myr, the degradation rate decreases by one order of magnitude. However, as the crater ages, the external surface gradually stabilizes. The sediments become less important to the crater filling, and the filling rate slows down considerably.

The erosion rates between Class 3 to 7 craters, as listed in Table 4, do not change significantly and stabilize at a low rate. This is probably because the abrasive effect of wind and sand on the crater rims is no longer evident as the crater floor is filled. And the rim erosion rate slowly decreases as the number of movable sediments decreases and the slope of the crater walls decreases. The fit to the rim height of the three deepest craters in each bin within the study area results in $h = 0.232D^{0.710}$ (Fig. 10d). Based on which fresh crater formation early erosion rates can reach ~ 0.030 m/Myr. As expected, both rim erosion rates and depth degradation rates decreased with increasing mean time scales.

Surface erosion rates calculated for the study area on the Middle to Late Amazonian time scale of our study are approximately 10^{-2} to10^{-3} m/Myr. Compared with Saunders and Young's (1983) erosion rates of 10^{-3} to 10^{-4} m^2/yr for a global compilation of Earth, the Martian surface erosion rate during the Middle to Late Amazonian is 2 orders of magnitude slower. But it is similar to the erosion rate of the lunar surfaces (Fassett and Combellick 2014). This suggests that surface erosion on Mars since the Middle Amazonian may be occurred in a dry, wind-driven environment with inefficient erosion processes due to the absence of the involvement of liquid water.

Conclusions

We mapped all craters ($D \geq 19$ m) over an area of approximately 134 km^2 in the Tianwen-1 landing zone, and classified each mapped crater according to its preservation states and morphological details. A high-resolution digital elevation model derived from HiRISE images was used to extract the depth and rim height of each crater by establishing a semi-automatic measurement method. The dependence of the morphometric parameters of the craters on the geological environment, as well as the

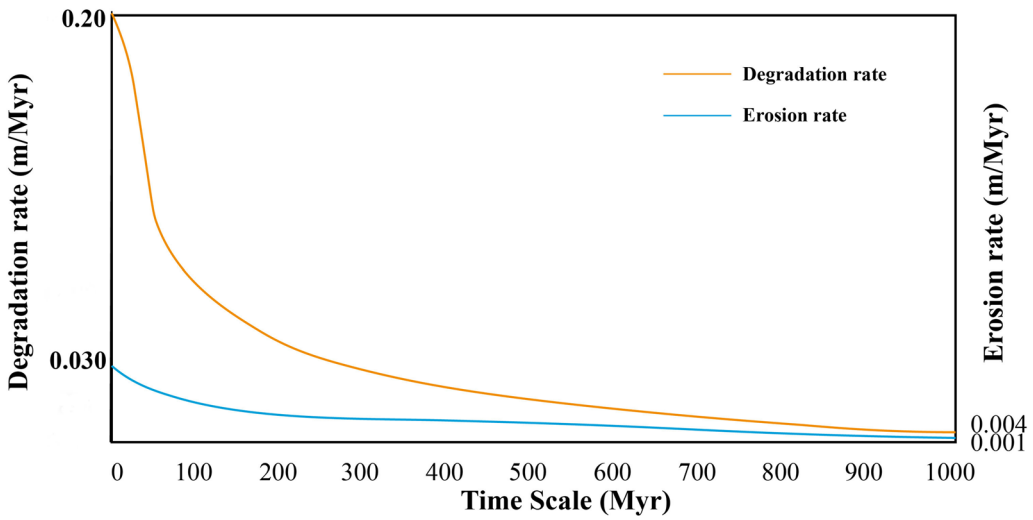

Fig. 11 Timeline of degradation and erosion rate changes for craters with 100 m diameter in the study area. The orange line represents the change in crater degradation rate with time and the blue line represents the change in erosion rate

degradation and erosion rates of the craters, are also analyzed and discussed. The conclusions are as follows.

1) Possible reasons for the discrepancy between our crater depth measurements and previous studies are that the d/D of fresh craters decreases rapidly, or that the craters we studied contain large populations of distant secondary impact craters. Impact events that occur in poorly cohesive weathering layers but fail to excavate the more competent bedrock beneath them can also result in smaller d/D.
2) Early fresh crater depth decreases more rapidly and the degradation rate may reach 0.2 m/Myr. As the crater ages and the surface gradually stabilizes, the importance of sediments for crater filling diminishes and the filling rate slows down considerably.
3) The surface erosion rates calculated on the Middle to Late Martian Amazonian timescale in our study can reach 10^{-2} to 10^{-3} m/Myr, comparable to surface erosion rates of 0.003 to 20 mm/year in arid and semi-arid regions on the Earth (Rohrmann et al. 2013). Our study area exhibits significantly lower wind erosion rates compared to those in arid and semi-arid regions on Earth. The findings indicate that the erosion processes in the study area is inefficiency, attributed to the absence of a substantial atmosphere and recent high-energy water events. Erosion in this region is primarily governed by wind or aeolian processes.

Supplementary Information

The online version contains supplementary material available at https://doi.org/10.1186/s40623-024-01965-1.

Additional file 1: Fig. S1. Crater depth raster (1 m per pixel). Depth is calculated by fitting a 3D plain across the rim using the points shown. Each point is assigned an elevation value from the HiRISE DEM. The DEM is then subtracted from the overlying 3D surface. Note: (e) is the 3D representation of (d). **Fig. S2.** Crater rim height raster (1 m per pixel) with the 0.2D annular region that generally defines the majority of the rim structure for all craters. Rim height is calculated by fitting a plain across the continuous ejecta blanket (1D from crater rim). This 3D plane defines the pre- impact surface and is subtracted from the overlying DEM. Note: (g) is the 3D representation of (f). **Fig. S3.** (a) The low-frequency radar imaging profile, with the uppermost thick black line denoting the topography relative to the landing site. The dashed line above 10 m denotes the estimated bottom of the top layer presumably containing mainly regolith. The two solid lines at depths of around 30 and 80 m represent the contacts between the second and third layers and the base of the third layer, respectively. The two dashed lines at around 10 and 40 m deep roughly separate finer- and coarser-grained rocky blocks within the second and third layers, respectively. (b) The interpreted lithologic stratigraphy based on radar imaging. (c) The variation of dielectric permittivity with depth. (Image credit: Chao Li et al.; 2022, Nature).

Acknowledgements
This work is supported by the National Key Research and Development Program of China (2022YFF0711400, 2022YFF0503100), the Strategic Leading Science and Technology Special Project of Chinese Academy of Sciences (XDB41000000), the National Natural Science Foundation (42372277, 41772346) and the Shandong Provincial Natural Science Foundation (ZR2023MD010). The authors would like to thank editors for the suggestions to improve our manuscript. We would like to thank Abdallah Zaki and the anonymous reviewer who provided very helpful and useful suggestions for the manuscript. We are grateful to the team members of the Ground Research and Application System, and National Astronomical Observatory of China, who will contribute to data receiving, processing and release of the China's Mars Mission (Tianwen-1). We also acknowledge the HiRISE and MOLA operations and engineering staffs (past and present) for their diligent work, who have contributed to the success of the HiRISE and MOLA investigations.

Author contributions
Conceptualization, BL and YW; methodology, BL and YY; software, YW, YL and ZL; validation, ZL and SQ; resources, SC, SQ and CL; writing—original draft preparation, YY and YW; writing—review and editing, BL and YL; project administration, BL; funding acquisition, SC All authors have read and agreed to the published version of the manuscript.

Availability of data and materials
The HiRISE images and DEMs can be downloaded from the website (https://www.uahirise.org/).

Declarations

Competing interests
We declare that we have no financial and personal relationships with other people or organizations that can inappropriately influence our work, there is no professional or other personal interest of any nature or kind in any product, service and/or company that could be construed as influencing the position presented in or the review of the manuscript entitled.

Author details
[1]Shandong Provincial Key Laboratory of Optical Astronomy and Solar-Terrestrial Environment, Institute of Space Sciences, Shandong University, Weihai, China. [2]College of Geoexploration Science and Technology, Jilin University, Changchun, China. [3]State Key Laboratory of Space Weather, National Space Science Center, Chinese Academy of Sciences, Beijing 100190, China. [4]Beijing Institute of Spacecraft System Engineering, Beijing 100094, China.

Received: 18 August 2023 Accepted: 9 January 2024
Published online: 29 January 2024

References

.
Daubar IJ, Mcewen AS, Byrne S, Kennedy MR, Ivanov B (2013) The current Martian cratering rate. Icarus 225(1):506–516
Daubar IJ, Atwood-Stone C, Byrne S, Mcewen AS, Russell PS (2014) The morphology of small fresh craters on Mars and the Moon. J Geophy Res Planets 119(12):2620–2639
Ding L, Zhou R, Yu T, Gao H, Yang H, Li J et al (2022) Surface characteristics of the zhurong mars rover traverse at utopia planitia. Nat Geosci 15(3):171–176. https://doi.org/10.1038/s41561-022-00905-6
Fassett CI, Combellick JR (2014). The rate of crater degradation and topographic evolution on the moon: results from the maria and initial comparisons with the highlands. Lunar and Planetary Science Conference.

Garvin JB, Sakamoto SEH, Frawley JJ (2003) Craters on mars: global geometric properties from gridded MOLA topography. Paper Presented at 6th International Conference on Mars. Calif. Inst. of Technology, Pasadena.
Golombek MP, Warner NH, Ganti V, Lamb MP, Parker TJ, Fergason RL, Sullivan R (2014) Small crater modification on Meridiani Planum and implications for erosion rates and climate change on Mars. J Geophys Res Planets 119(12):2522–2547. https://doi.org/10.1002/2014JE004658
Grant JA, Warner NH, Weitz CM, Golombek MP, Wilson SA, Baker M, Hauber E, Ansan V, Charalambous C, Williams N, Calef F, Pike WT, DeMott A, Kopp M, Lethcoe H, Banks ME (2020) Degradation of homestead hollow at the InSight landing site based on the distribution and properties of local deposits. J Geophys Res Planets 125(4):e2019JE006350. https://doi.org/10.1029/2019JE006350
Hartmann WK, Neukum G (2001) Cratering chronology and the evolution of Mars. Space Sci Rev 96(1–4):165–194
Ivanov BA (2001) Mars/Moon cratering rate ratio estimates. Space Sci Rev 96(1):87–104
Ivanov MA, Hiesinger H, Erkeling G, Reiss D (2014) Mud volcanism and morphology of impact craters in Utopia Planitia on mars: evidence for the ancient ocean. Icarus 228:121–140
Johnston D, Graf JE, Zurek RW, Eisen HJ, Jai B (2003)The Mars reconnaissance orbiter mission, 2003 IEEE Aerospace Conference Proceedings (Cat. No.03TH8652), Big Sky, MT, USA vol.1, pp. 1–204. Doi: https://doi.org/10.1109/AERO.2003.1235052.
Kirk RL et al (2008) Ultrahigh resolution topographic mapping of Mars with MRO HiRISE stereo images: meter-scale slopes of candidate Phoenix landing sites. J Geophys Res 113:E00A24. https://doi.org/10.1029/2007JE003000
Kneissl T, Neukum SVG (2011) Map-projection-independent crater size-frequency determination in GIS environments-New software tool for ArcGIS. Planet Space Sci 59(11–12):1243–1254
Li C, Zheng Y, Wang X et al (2022) Layered subsurface in Utopia Basin of Mars revealed by Zhurong rover radar. Nature 610:308–312. https://doi.org/10.1038/s41586-022-05147-5
Liu Y, Wu X, Zhao Y-YS, Pan L, Wang C, Liu J, Zhao Z, Zhou X, Zhang C, Wu Y, Wan W, Zou Y (2022) Zhurong reveals recent aqueous activities in Utopia Planitia Mars. Sci Adv 8(19):8555. https://doi.org/10.1126/sciadv.abn8555
Mcewen AS, Eliason EM, Bergstrom JW, Bridges NT, Hansen CJ, Delamere WA, Grant JA, Gulick VC, Herkenhoff KE, Keszthelyi L (2007) Mars reconnaissance orbiter's high-resolution imaging science experiment (HiRISE). J Geophys Res Atmosph 112(E5):5
Melosh HJ (1989) Impact cratering: a geologic process. New York: Oxford University Press; Oxford: Clarendon Press.
Michael GG (2013) Planetary surface dating from crater size–frequency distribution measurements: Multiple resurfacing episodes and differential isochron fitting. Icarus 226(1):885–890
Michael GG, Neukum G (2010) Planetary surface dating from crater size–frequency distribution measurements: Partial resurfacing events and statistical age uncertainty. Earth Planet Sci Lett 294(3–4):223–229
Pike RJ, Wilhelms DE (1978). Secondary-impact craters on the moon: topographic form and geologic process. lunar and planetary science conference. LPI.
Pike RJ (1977). Size-dependence in the Shape of Fresh Impact Craters on the Moon, In: DJ Roddy, RO Pepin, and RB Merrill (eds.), Impact and Explosion Cratering, Pergamon; New York, pp. 489–509.
Robbins SJ, Hynek BM (2012) A new global database of Mars impact craters ≥1 km: 2. Global crater properties and regional variations of the simple-to-complex transition diameter. J Geophys Res 117:06001. https://doi.org/10.1029/2011JE003967
Rohrmann A, Heermance R, Kapp P, Cai F (2013) Wind as the primary driver of erosion in the Qaidam Basin. China Earth Planet Sci Lett 374:1–10
Saunders I, Young A (1983) Rates of surface processes on slopes, slope retreat and denudation. Earth Surf Proc Land 8(5):473–501. https://doi.org/10.1002/esp.329008050
Searls ML, Banerdt WB, Phillips RJ (2006) Utopia and hellas basins, mars: twins separated at birth. J Geophys Res 111:E08005. https://doi.org/10.1029/2005JE002666
Stewart ST, Valiant GJ (2006) Martian subsurface properties and crater formation processes inferred from fresh impact crater geometries. Meteorit Planet Sci 41(10):1509–1537
Sweeney J, Warner NH, Ganti V, Golombek MP, Lamb MP, Fergason R, Kirk R (2018) Degradation of 100-m-scale rocky ejecta craters at the InSight landing site on mars and implications for surface processes and erosion rates in the hesperian and amazonian. J Geophys Res Planets 123(10):2732–2759. https://doi.org/10.1029/2018JE005618
Tanaka KL, Robbins SJ, Fortezzo CM, Skinner JA, Hare TM (2014) The digital global geologic map of Mars: chronostratigraphic ages, topographic and crater morphologic characteristics, and updated resurfacing history. Planet Space Sci 95(may):11–24
Warner NH, Grant JA, Wilson SA, Golombek MP, DeMott A, Charalambous C, Hauber E, Ansan V, Weitz C, Pike T, Williams N, Banks ME, Calef F, Baker M, Kopp M, Deahn M, Lethcoe H, Berger L (2020) An Impact crater origin for the InSight landing site at homestead hollow, mars: implications for near surface stratigraphy, surface processes, and erosion rates. J Geophys Res Planets 125(4):e2019JE006333. https://doi.org/10.1029/2019JE006333
Watters WA, Geiger LM, Fendrock M, Gibson R (2015) Morphometry of small recent impact craters on Mars: size and terrain dependence, short-term modification. J Geophys Res Planets 120(2):226–254. https://doi.org/10.1002/2014JE004630
Zaki AS, Edgett KS, Pajola M, Kite E, Davis JM, Mangold N et al (2023) Prolonged record of hydroclimatic changes at Antoniadi crater Mars. J Geophys Res Planets 128:2022007606. https://doi.org/10.1029/2022JE007606
Zhao J, Xiao Z, Huang J, Head JW, Wang J, Shi Y, Wu B, Wang L (2021) Geological characteristics and targets of high scientific interest in the zhurong landing region on mars. Geophys Res Lett 48(20):e2021GL094903. https://doi.org/10.1029/2021GL094903
Zou Y, Zhu Y, Bai Y, Wang L, Peng Y (2021) Scientific objectives and payloads of Tianwen-1, China's first Mars exploration mission. Adv Space Res 67(2):812–823. https://doi.org/10.1016/j.asr.2020.11.005

Publisher's Note